

# Comprehensive study of the global phase diagram of the $J$ - $K$ - $\Gamma$ model on a triangular lattice

Shi Wang<sup>1</sup>,<sup>1</sup> Zhongyuan Qi,<sup>2</sup> Bin Xi,<sup>2</sup> Wei Wang<sup>3</sup>,<sup>3</sup> Shun-Li Yu<sup>1,4,\*</sup> and Jian-Xin Li<sup>1,4,†</sup>

<sup>1</sup>National Laboratory of Solid State Microstructures and School of Physics, Nanjing University, Nanjing 210093, China

<sup>2</sup>College of Physics Science and Technology, Yangzhou University, Yangzhou 225002, China

<sup>3</sup>School of Science, Nanjing University of Posts and Telecommunications (NUPT), Nanjing 210023, China

<sup>4</sup>Collaborative Innovation Center of Advanced Microstructures, Nanjing University, Nanjing 210093, China



(Received 6 September 2020; revised 19 January 2021; accepted 25 January 2021; published 4 February 2021)

The celebrated Kitaev honeycomb model provides an analytically tractable example with an exact quantum spin liquid ground state. While in real materials, other types of interactions besides the Kitaev coupling ( $K$ ) are present, such as Heisenberg ( $J$ ) and symmetric off-diagonal ( $\Gamma$ ) terms, these interactions can also be generalized to a triangular lattice. Here, we carry out a comprehensive study of the  $J$ - $K$ - $\Gamma$  model on a triangular lattice covering the whole parameter region, using a combination of exact diagonalization, classical Monte Carlo, and analytic methods, with an emphasis on the effects of the  $\Gamma$  term. In the HK limit ( $\Gamma = 0$ ), we find five quantum phases which are quite similar to their classical counterparts. Among them, stripe-A and dual Néel phases are robust against the introduction of the  $\Gamma$  term, in particular, stripe A extends to the region connecting  $K = -1$  and  $K = 1$  for  $\Gamma < 0$ . Though the  $120^\circ$  Néel phase also extends to a finite  $\Gamma$ , its region is largely reduced compared to the previous classical result. Interestingly, the ferromagnetic (dubbed FM-A) and stripe-B phases are unstable in response to an infinitesimal  $\Gamma$  interaction. Moreover, we find five additional phases for  $\Gamma \neq 0$  which are elaborated by both the quantum and classical numerical methods. Part of the parameter space previously identified as the  $120^\circ$  Néel phase in the classical study is found to give way to the modulated stripe phase. Depending on the sign of the  $\Gamma$  term, the FM-A phase transits into FM-B ( $\Gamma > 0$ ) and FM-C ( $\Gamma < 0$ ) phases with different spin orientations. Similarly, the stripe-B phase transits into stripe-C ( $\Gamma > 0$ ) and stripe-A ( $\Gamma < 0$ ) phases. Around the positive  $\Gamma$  point, due to the interplay of the Heisenberg, Kitaev, and  $\Gamma$  interactions, we find a possible quantum spin liquid in a noticeable region with a continuum in spin excitations.

DOI: [10.1103/PhysRevB.103.054410](https://doi.org/10.1103/PhysRevB.103.054410)

## I. INTRODUCTION

Geometric frustration, which arises when the lattice geometry gives rise to constraints that not every exchange bond can be simultaneously minimized in energy, plays an important role in various kinds of magnetic systems. The nearest-neighbor (NN) antiferromagnetic (AFM) Heisenberg model on the triangular lattice is a typical example; once two of the spins on an elementary triangle are antiparallel to satisfy their AFM interaction, the third one can no longer point in a direction opposite to both other spins. In particular, the spin-1/2 case has attracted much interest and was extensively studied after the seminal prediction by Anderson of a quantum spin liquid (QSL) where a strong quantum fluctuation prevents any long-range order down to zero temperature [1], although it has been shown by later studies that the ground state (GS) has a classical magnetic order with each spin on a triangle pointing to  $120^\circ$  with respect to each other [2–5]. When the interactions beyond the NN Heisenberg type are included which introduce further frustration, the system has a much richer phase diagram including the  $120^\circ$  Néel state, stripe states, and QSL states [6–18]. All these studies have revealed that

geometric frustrated systems show quite different behavior from that of nonfrustrated systems.

On the other hand, exchange frustration in systems with strongly anisotropic magnetic interactions has been shown to be another promising approach to explore exotic quantum spin states. Like geometric frustration, the effect of exchange frustration is to prevent the formation of long-range magnetic order and give rise to a residual GS entropy. The spin-1/2 Kitaev model [19] on a honeycomb lattice, which has both gapped and gapless QSL states supporting fractionalized excitations, is a celebrated example of a model with exchange frustration. In this model, the spins subject to the Kitaev interactions consist of NN Ising-type interactions, with the quantization axis depending on the spatial orientation of an exchange bond. Because of its theoretical importance and potential applications in quantum computing, great efforts have been made to search for a solid-state realization of the Kitaev model. Khaliullin and Jackeli [20,21] proposed that this highly anisotropic Kitaev interaction can be realized in  $4d/5d$  systems with a low spin state of  $d^5$  configuration, such as iridates  $A_2\text{IrO}_3$  ( $A = \text{Na}, \text{Li}$ ). In these systems, the bond-directional interactions originate from the joint effects of strong spin-orbital coupling, electron interactions,  $d^5$  configurations, and  $90^\circ$  bond geometry formed by edge-sharing octahedra. However, in real materials, other types of interactions besides the Kitaev coupling are present and these interactions may induce other interesting ordered and

\*Email address: slyu@nju.edu.cn

†Email address: jxli@nju.edu.cn

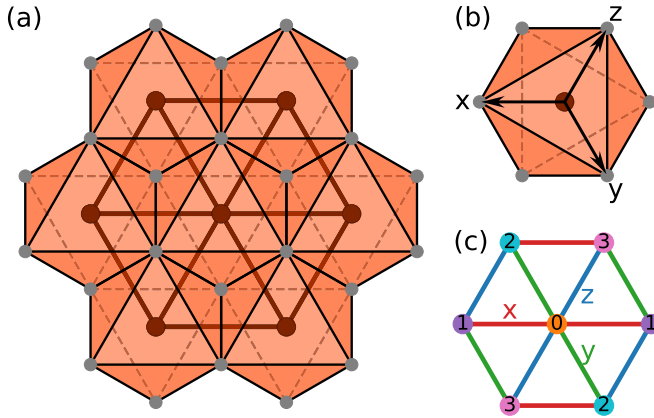


FIG. 1. (a) Top view of the triangular lattice of the edge-sharing octahedron. (b) The orientation of the cubic  $x$ ,  $y$ ,  $z$  axes with respect to the octahedron. The spin operators  $S^x$ ,  $S^y$ , and  $S^z$  are defined with respect to this reference frame. (c) Three types of the NN bonds on the triangular lattice, namely,  $\gamma = x, y, z$  colored red, green, and blue, respectively. The different colors of the lattice sites label the four sublattices realizing the four-sublattice transformation (see main text for details).

disordered phases. The simplest extension of the pure Kitaev model is the Heisenberg-Kitaev (HK) model [22,23], in which the NN Heisenberg interaction is also taken into account. This model has been extensively studied by various numerical methods [24–28], which revealed the presence of four magnetically ordered phases with collinear spin patterns of ferromagnetic (FM), AFM, stripe, and zigzag types, besides extended spin-liquid phases near the Kitaev limits. Considering the most idealized crystal structure, another interaction beyond the HK model also must be included, i.e., bond-dependent symmetric off-diagonal exchange, which is called the  $\Gamma$  interaction [29–31]. Thus, the generic NN exchange Hamiltonian for the undistorted hexagonal compounds is the  $J$ - $K$ - $\Gamma$  model, where the Heisenberg ( $J$ ), Kitaev ( $K$ ), and  $\Gamma$  interactions are all included. Finite  $\Gamma$  further enriches the phase diagram by adding noncollinear and incommensurate spiral phases [29,32,33]. Moreover, in real materials, such as  $A_2\text{IrO}_3$  and  $\alpha\text{-RuCl}_3$ , the dominant interactions are the  $\Gamma$  and FM Kitaev terms which originate from both direct  $d$ - $d$  and anion-mediated  $d$ - $p$  electron transfer, while the Heisenberg term has the smallest strength since it predominantly originates from the weak direct  $d$ - $d$  electron transfer [30,31].

In fact, magnetic ions located at the center of edge-sharing octahedra cannot only form the honeycomb lattice but also the triangular lattice [see Fig. 1(a)], so the Kitaev and  $\Gamma$  terms can naturally be generalized to the triangular lattice [34,35]. On the experimental side, studies on several classes of compounds containing localized  $4d$ ,  $5d$ , or  $4f$  electrons have recently shown that the quantum spin model on the triangular lattice can be formed by the localized moments [36–42]. In particular, due to their possible Kramers doublets and spin-orbital coupling, these moments can be treated as  $S_{\text{eff}} = 1/2$  at low temperatures, and the spin-orbital entanglement can induce direction-dependent exchanges, such as the  $K$  and  $\Gamma$  terms. A typical example is  $\text{YbMgGaO}_4$  [38,39], in which the  $\text{Yb}^{3+}$  ions form a triangular layer and

are surrounded by  $\text{O}^{2-}$ , which construct edge-sharing octahedra, but due to the inherent disorder effect there are still controversies about the GS of this material [38–40,43–49]. More recently, an alternative family of compounds  $\text{ARCh}_2$  ( $A$ =alkali,  $R$ =rare-earth,  $\text{Ch}=\text{O}, \text{S}, \text{Se}$ ) with perfect triangular lattices of rare-earth ions have been synthesized and explored. The magnetic susceptibility and heat capacity data suggest no long-range magnetic order or spin freezing down to the lowest measurement temperature, which implies their candidacy for a QSL state [50–56]. These triangular magnets provide suitable platforms to study the interplay of geometric frustration and exchange frustration induced by spin-orbital couplings.

The phase diagram of the HK model ( $\Gamma = 0$ ) on the triangular lattice has been studied by means of Luttinger-Tisza minimization together with classical Monte Carlo simulation [35], exact diagonalization (ED) [57,58], and density matrix renormalization group [59,60]. All these methods give consistent results about four magnetically ordered phases: two collinear patterns of FM and stripe types and two noncollinear patterns of  $120^\circ$  Néel and noncoplanar spiral types. Note that the distortions of the  $120^\circ$  Néel order, when the model deviates from the AFM Heisenberg limit ( $K = 0, J > 0$ ), were also called the  $Z_2$  vortex crystal [35,58,59,61,62]. However, the nature of the phase around the AFM Kitaev point is still under debate. The Luttinger-Tisza minimization method suggested it to be a  $Z_2$  vortex crystal [35], the Schwinger-fermion mean-field theory proposed it to be a QSL [57], the Schwinger-boson mean-field theory thought it to be a nematic phase [63], while the density matrix renormalization group calculations suggested it to be a nematic phase [58,59] or a stripe phase [60]. When the symmetric off-diagonal  $\Gamma$  interaction is included, a classical analysis reveals that the stripe and FM phases dominate the  $J$ - $K$ - $\Gamma$  phase diagram, in addition to small regions of  $120^\circ$  Néel,  $Z_2$  vortex crystal, and nematic phases [64]. However, the studies on the effects of quantum fluctuations on the global  $J$ - $K$ - $\Gamma$  phase diagram are scarce. In particular, since no exact solution has been reported so far for the pure spin-1/2 Kitaev and  $\Gamma$  models on the triangular lattice, it also remains conceptually interesting to investigate whether QSL states could exist as possible GSs due to quantum fluctuations introduced by these exchange-frustrated interactions.

In this paper, we study the global phase diagram and the phase transitions of the triangular lattice  $J$ - $K$ - $\Gamma$  model using a combination of ED, classical simulation, and analytical analyses. In the HK limit ( $\Gamma = 0$ ), there are five classical phases: one FM, two stripe, one  $120^\circ$  Néel, and its dual phase. For the pure AFM Kitaev model, although the system has highly degenerate classical GSs composed of stripe and nematic states, the order-by-disorder mechanism caused by quantum fluctuations makes the system select the stripe state to be the GS. When the  $\Gamma$  term is included, we find five additional phases: two FM, one stripe, one modulated stripe, and one possible QSL phase. With the aid of classical analysis, we determine the spin configuration for each magnetically ordered phase and explain why there are phase transitions between the phases with the same types of classical orders. On the other hand, we find that the order-by-disorder mechanism makes the GSs of the pure  $\Gamma$  models have FM orders, although the classical analyses suggest that the GSs are highly degenerate.

For the possible QSL phase, based on the investigation of the spin excitation spectrum, we suggest the GS is a gapped  $Z_2$  QSL.

## II. MODEL AND METHODS

### A. Model

The  $J$ - $K$ - $\Gamma$  model Hamiltonian on the triangular lattice is given by

$$H = \sum_{(i,j) \in \alpha\beta(\gamma)} [JS_i \cdot S_j + KS_i^\gamma S_j^\gamma + \Gamma(S_i^\alpha S_j^\beta + S_i^\beta S_j^\alpha)], \quad (1)$$

where  $(i, j)$  denotes the NN bonds,  $\gamma$  takes value  $x, y$ , or  $z$  depending on the direction of the NN bond as shown in Fig. 1(c), and  $\alpha, \beta$  are the remaining directions.  $J$  and  $K$  are the magnitude of the Heisenberg and Kitaev interactions and  $\Gamma$  the symmetric off-diagonal exchange.

In the following, for convenience, we fix the energy scale with  $\sqrt{J^2 + K^2 + \Gamma^2} = 1$  and parametrize the exchange parameters using spherical angles  $\alpha$  and  $\beta$ ,

$$J = \sin \alpha \sin \beta, \quad K = \sin \alpha \cos \beta, \quad \Gamma = \cos \alpha, \quad (2)$$

where  $\alpha \in [0, \pi]$  and  $\beta \in [0, 2\pi]$  to cover the global parameter space.

In the HK limit ( $\Gamma = 0$ ), the model Eq. (1) admits an exact duality transformation, i.e., the so-called four-sublattice-transformation (FST) [34]. The FST is a spin rotation transformation which divides the triangular lattice into four sublattices [see Fig. 1(c)] and performs the following rotations of the spins on the four sublattices to map the spin  $S_i$  to  $S'_i$ :

$$\begin{aligned} S'_0 &= S_0 && \text{for sublattice 0,} \\ S'_1 &= (S_1^x, -S_1^y, -S_1^z) && \text{for sublattice 1,} \\ S'_2 &= (-S_2^x, S_2^y, -S_2^z) && \text{for sublattice 2,} \\ S'_3 &= (-S_3^x, -S_3^y, S_3^z) && \text{for sublattice 3.} \end{aligned} \quad (3)$$

This corresponds to a  $\pi$  rotation around  $x, y$ , and  $z$  axes for the spin operators on the sublattices 1, 2, and 3, respectively. The resulting Hamiltonian  $H'(S')$  has the same form as the original Hamiltonian albeit with different model parameters:

$$J' = -J, \quad K' = 2J + K. \quad (4)$$

For the spherical angles defined in Eqs. (2), the mapping takes the form

$$\tan \beta' = -\sin \beta / (2 \sin \beta + \cos \beta). \quad (5)$$

This special property of the model can help us to identify some exotic magnetically ordered phases from the well-established simple counterparts.

### B. Exact diagonalization method

To obtain the quantum phase diagram of the model Eq. (1), we perform ED calculations of the GS of the Hamiltonian Eq. (1) on a  $4 \times 6$  cluster with the periodic boundary condition. To detect quantum phase transitions, the second derivatives of the GS energy,  $-\partial^2 E_0 / \partial \alpha^2$  and  $-\partial^2 E_0 / \partial \beta^2$ ,

were computed and their singularities are used to identify possible phase transitions.

To identify the GS properties, we first examine the static structure factor (SSF),

$$\mathcal{S}(\mathbf{Q}) = \frac{1}{N} \sum_{ij} \langle \Omega | S_i \cdot S_j | \Omega \rangle e^{i\mathbf{Q} \cdot (\mathbf{R}_i - \mathbf{R}_j)}, \quad (6)$$

from which we can find the wave vectors of the ordered phases and distinguish possible QSL states. Here,  $|\Omega\rangle$  is the GS,  $N$  is the total number of lattice sites, and  $\mathbf{R}_i$  the position of site  $i$ .

To further determine the magnetic configurations of the magnetically ordered phases, we employ a method by studying the projections of the exact GSs of the finite cluster to the classical states [65]. The basic idea of this method is to measure the probabilities of the cluster spin coherent states in the exact cluster GS with varying moment directions. The cluster spin coherent state is a direct product of spin-1/2 coherent states on each site  $i$ , i.e.,

$$|\Psi\rangle = \bigotimes_{i=1}^N |\theta_i, \phi_i\rangle, \quad (7)$$

where the spin-1/2 coherent state

$$|\theta, \phi\rangle = \mathcal{R}_z(\phi) \mathcal{R}_y(\theta) |\uparrow\rangle = e^{-i\phi S^z} e^{-i\theta S^y} |\uparrow\rangle \quad (8)$$

is fully polarized state along the  $(\theta, \phi)$  direction. Here the cubic axes are used [see Fig. 1(b)];  $\theta$  and  $\phi$  are the conventional spherical angles. By calculating the overlap between the exact cluster GS and cluster spin coherent states,  $P = |\langle \Psi | \text{GS} \rangle|^2$ , and maximizing its value with respect to  $\theta$ 's and  $\phi$ 's, we can then identify the classical spin pattern that best fits the exact quantum GS.

Since one of the key characteristics of QSL is the fractional excitation, which can lead to a continuous spectrum, we study the dynamic structure factor (DSF)  $A(\mathbf{k}, \omega)$  to search for the possible QSLs.  $A(\mathbf{k}, \omega)$  is given by

$$A(\mathbf{k}, \omega) = -\frac{1}{\pi} \text{Im} \mathcal{S}(\mathbf{k}, \omega), \quad (9)$$

$$\mathcal{S}(\mathbf{k}, \omega) = \frac{1}{N} \sum_{ij} S_{ij}(\omega) e^{i\mathbf{k} \cdot (\mathbf{R}_i - \mathbf{R}_j)}, \quad (10)$$

$$S_{ij}(\omega) = \langle \Omega | S_i^+ \frac{1}{\omega + i0^+ - H + E_0} S_j^- | \Omega \rangle, \quad (11)$$

where  $E_0$  is the GS energy.

### C. Classical Monte Carlo method

To better understand the quantum phases identified by the ED method, we also perform classical Monte Carlo simulations. We begin with parallel-tempering Monte Carlo [66] on 40 replicas with temperature  $T/J$  ranging from 0.001 to 1.0. For each replica, we sample it with a combination of heat-bath [67] and over-relaxation methods [68], mainly on a  $24 \times 24$  triangular lattice with periodic boundary condition. A whole Monte Carlo step consists of a single heat-bath sweep and, subsequently, ten over-relaxation sweeps over the entire lattice. We perform  $10^6$  Monte Carlo steps per replica, then, we copy out the spin configuration from the lowest- $T$  replica, and sample it with a combination of zero-temperature

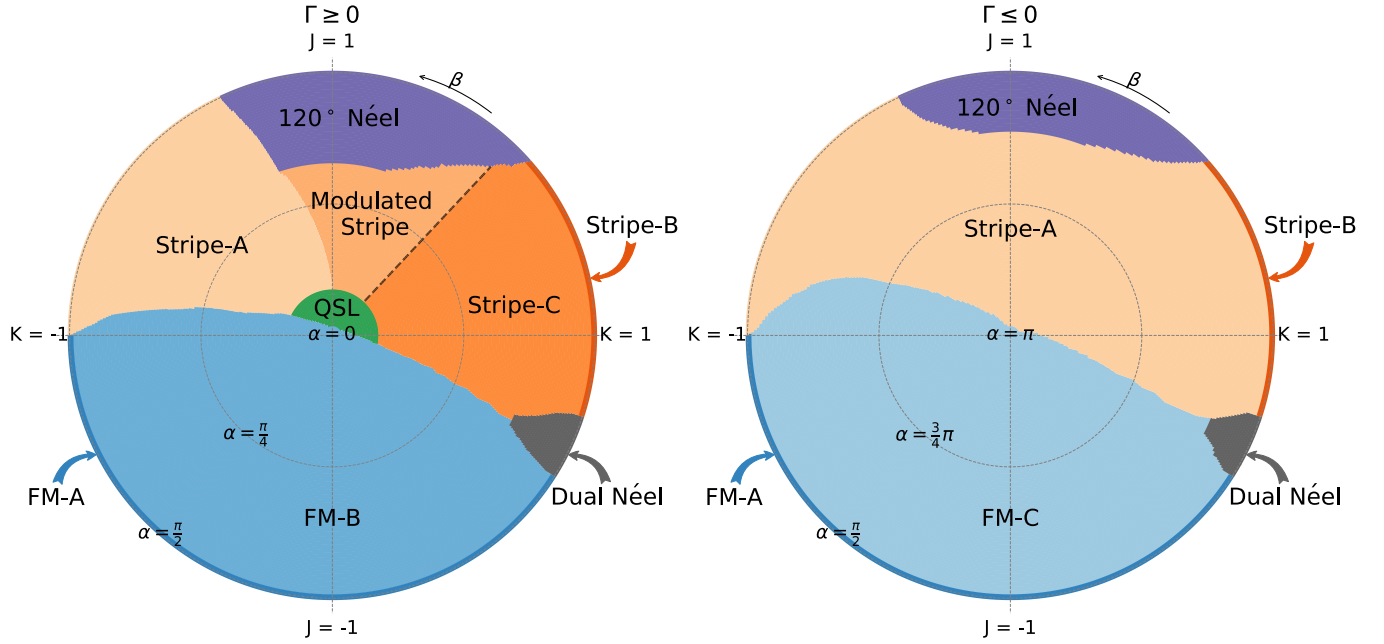


FIG. 2. Zero-temperature global phase diagram of the triangular lattice  $J$ - $K$ - $\Gamma$  model. Angles  $\alpha$  and  $\beta$  denote the radial and azimuthal angles, respectively. There are in total ten phases including three FM phases denoted FM-A, FM-B and FM-C, three stripe phases denoted stripe A, stripe B, and stripe C, a modulated stripe phase, a  $120^\circ$  Néel phase, a dual Néel phase, and a possible QSL phase. Phase boundaries are determined by the singularities of  $-\partial^2 E_0 / \partial \alpha^2$  and  $-\partial^2 E_0 / \partial \beta^2$  from ED calculations except for that depicted by the dashed line between the modulated stripe and stripe-C phases given by classical analyses.

heat-bath and over-relaxation methods to get the GS. The zero-temperature heat-bath sampling is simply aligning the spins according to their local fields:

$$\vec{S}_i = \frac{\vec{h}_i^{\text{loc}}}{|\vec{h}_i^{\text{loc}}|} S, \quad (12)$$

with

$$\vec{h}_i^{\text{loc}} = \sum_{\langle j \rangle} J \vec{S}_j + K S_j^\gamma \hat{e}^\gamma + \Gamma (S_j^\alpha \hat{e}^\beta + S_j^\beta \hat{e}^\alpha), \quad (13)$$

and the over-relaxation sampling is just a mirror reflection of a spin with respect to the local field:

$$\vec{S}_i^{\text{new}} = \frac{2(\vec{S}_i^{\text{old}} \cdot \vec{h}_i^{\text{loc}}) \vec{h}_i^{\text{loc}}}{|\vec{h}_i^{\text{loc}}|^2} - \vec{S}_i^{\text{old}}. \quad (14)$$

For some competing states, we start from several different initial configurations to obtain the correct classical GS.

From the magnetic configuration of GSs, we compute the SSF given by

$$S_k = \frac{1}{N} \sum_{ij} \langle \vec{S}_i \cdot \vec{S}_j \rangle e^{ik \cdot (r_i - r_j)}, \quad (15)$$

which is a key characteristic to identify magnetic phases.

### III. RESULTS

#### A. Global phase diagram

The zero-temperature quantum phase diagrams obtained by the ED method for  $\Gamma \geq 0$  and  $\Gamma \leq 0$  on a  $4 \times 6$  cluster with the periodic boundary condition are presented in Fig. 2,

where the phase boundaries are determined by the location of singularities in  $-\partial^2 E_0 / \partial \alpha^2$  and  $-\partial^2 E_0 / \partial \beta^2$  (see Appendix A for details). We find nine magnetically ordered phases and a phase ascribed to be a QSL. The nine ordered magnetic phases consist of three stripe phases (dubbed stripe A, stripe B, and stripe C in Fig. 2), three FM phases (dubbed FM-A, FM-B, and FM-C in Fig. 2), one  $120^\circ$  Néel phase, one dual Néel phase, and one modulated stripe phase. In the following, we will discuss the details on the nature of these phases and the corresponding phase transitions.

Let's first discuss the HK limit for  $\Gamma = 0$ . In accord with the previous study [57], we find five quantum phases (see Fig. 3). For pure Heisenberg models ( $K = \Gamma = 0$ ), the GSs are

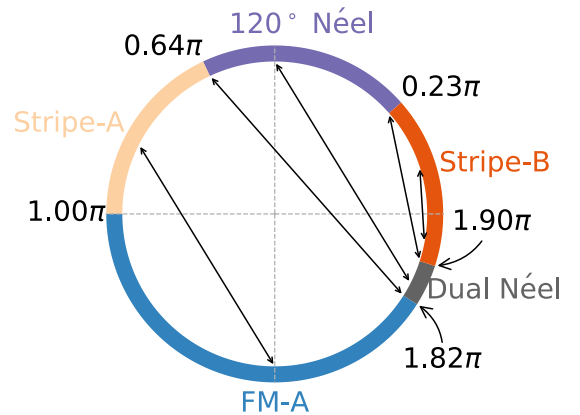


FIG. 3. Phase diagram in the HK limit ( $\Gamma = 0$ ). The double-arrow lines are the representative lines that connect the points exactly related by the FST.



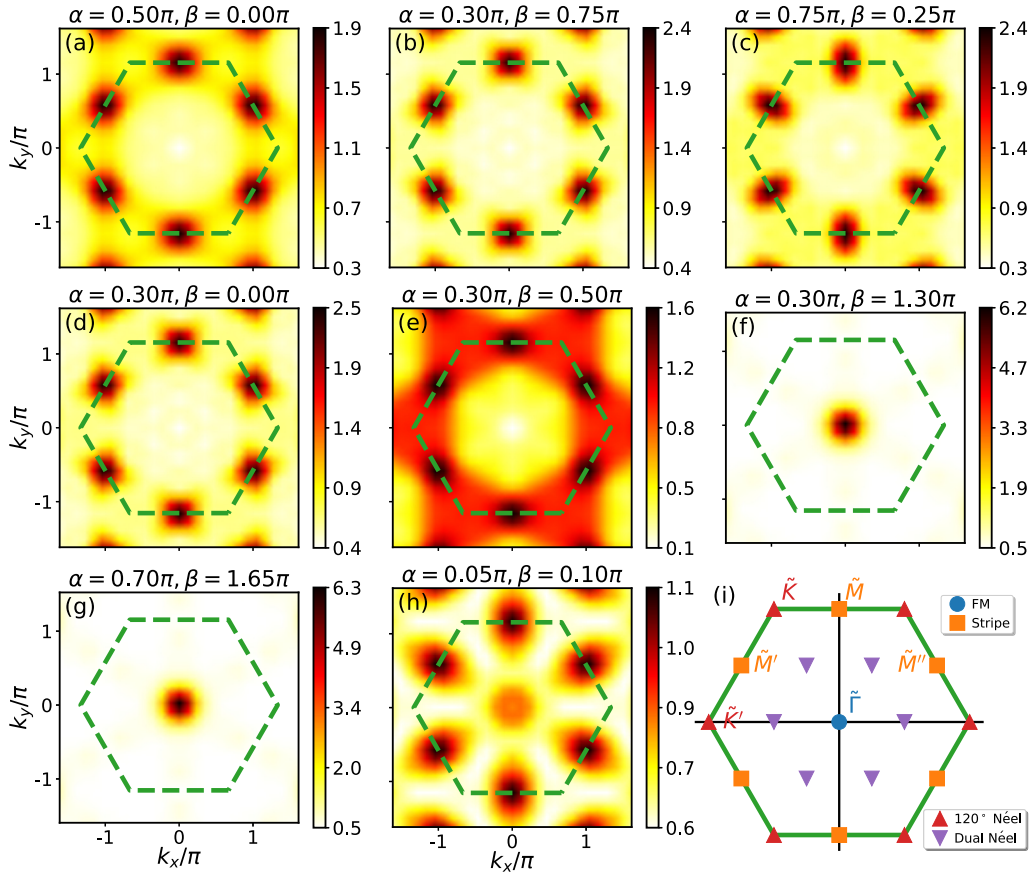


FIG. 4. SSFs from the ED calculations for representative interaction parameters in different phases: (a) stripe B, (b) and (c) stripe A, (d) stripe C, (e) modulated stripe, (f) FM-B, (g) FM-C, (h) QSL. The green dashed lines mark the first BZ of the triangular lattice. (i) Characteristic wave vectors for the FM (blue circle), stripe (orange square),  $120^\circ$  Néel (red up-triangle), and dual Néel (purple down-triangle) phases. See Appendix C for the SSFs of the  $120^\circ$  Néel phase, dual Néel phase, and pure  $\Gamma$  models.

well known, i.e., a FM state for  $J < 0$  and a  $120^\circ$  Néel state for  $J > 0$ , respectively. So, the phase in the region between  $\beta = 1.00\pi$  and  $1.82\pi$  is identified as FM-A, and that between  $\beta = 0.23\pi$  and  $0.64\pi$  the  $120^\circ$  Néel state. As introduced in Sec. II A, the HK model ( $\Gamma = 0$ ) preserves its form under the FST, which is in fact a spin-rotation transformation [34]. The transformed model has different exchange interactions related to the original ones via Eq. (4) and the mapping angle is given by Eq. (5). Thus, by virtue of the FST, we can identify other two magnetically ordered phases. Starting from the FM-A phase, it will be transformed to the phase between  $\beta = 1.00\pi$  and  $0.64\pi$  via the angle mapping Eq. (5). Then, using the spin rotation transformation Eq. (3), one can identify the phase between  $\beta = 1.00\pi$  and  $0.64\pi$  as a collinear stripe state (denoted stripe-A). Similarly, the  $120^\circ$  Néel state is transformed to a noncollinear spiral order (dual Néel) in the region from  $\beta = 1.82\pi$  to  $\beta = 1.90\pi$ . We also note that, as indicated in Fig. 3, the transition points  $\beta = 0.23\pi$  and  $0.64\pi$  are indeed mapped to the transition points  $\beta = 1.90\pi$  and  $1.82\pi$  through the FST. However, the transition point  $\beta = \pi$  is mapped to itself under the FST, so it is the isolated transition point.

For the phase near the AFM Kitaev point ( $J = \Gamma = 0$ ,  $K = 1$ ), which is between  $\beta = 1.90\pi$  and  $0.23\pi$ , the points in this phase are mapped to those in the same phase under the FST, so it was supposed to be a magnetically disordered phase [57]. However, as shown in Fig. 4(a), when checking the SSF

in this phase, we find that the SSF shows obvious peaks at the  $\tilde{M}$  points, which implies that it is likely to be a magnetically ordered phase. We further perform a basin-hopping global optimization [69] on a  $12 \times 12$  lattice by taking the spins as classical magnetic moments to search for the possible spin configurations under this set of interaction parameters. We find that there are two types of degenerate classical GSs, one of which has the stripe order and the other the nematic order, since the AFM chains are decoupled (see Appendix D for details). When we consider the quantum fluctuations generated by the Kitaev interactions not along the AFM chains, the fourth-order corrections will give an effective coupling between the next-NN spins [70], which can stabilize the stripe order. As shown in Fig. 4(i), the peaks of SSF of the classical stripe orders are also consistent with the result calculated from ED [see Fig. 4(a)]. Moreover, every stripe order in this phase (see Appendix D for details) can be transformed to another degenerate stripe pattern in the same phase by the spin rotation transformation of FST. Thus, the degeneracy of the spin configurations is lifted by the order-by-disorder mechanism, and we can identify that the phase containing the AFM Kitaev point of the HK model (between  $\beta = 1.90\pi$  and  $0.23\pi$ ) is a stripe phase, which we label stripe B.

Then, let us study the effects of the  $\Gamma$  term on the phase diagram. One may expect that the phases in the HK limit ( $\Gamma = 0$ ) would extend to a finite region in the global phase

diagram of the  $J$ - $K$ - $\Gamma$  model. Our ED results do show that the stripe-A phase can extend to a large region from  $\Gamma > 0$  to  $\Gamma < 0$ , in particular, it extends to the region connecting  $K = -1$  to  $K = 1$  for  $\Gamma < 0$ . The region of the dual Néel phase that was dubbed a dual- $Z_2$  vortex crystal phase in Ref. [64] also survives the introduction of the  $\Gamma$  term, though the region is much smaller than the stripe-A phase. These results are consistent qualitatively with the classical results [64]. However, we find that an infinitesimal  $\Gamma$  interaction can make the FM-A phase and the stripe-B phase unstable, so these two phases are actually phase boundaries in the global phase diagram. On the other hand, although the  $120^\circ$  Néel phase can also extend to a certain region, its area in the phase diagram is much smaller than the classical results [64]. Besides these phases that already exist in the HK limit, there are five additional phases, according to our ED calculations. Since the SSF is a key physical quantity to reveal the nature of each quantum phases, especially the spin configuration of the ordered phases, we will discuss the properties of the phases with  $\Gamma \neq 0$  in detail according to the SSFs.

In Figs. 4(b) and 4(c), we show the SSFs for two typical points in the stripe-A phase, i.e.,  $\alpha = 0.3\pi$ ,  $\beta = 0.75\pi$  and  $\alpha = 0.75\pi$ ,  $\beta = 0.25\pi$  in the  $\Gamma > 0$  and  $\Gamma < 0$  regions, respectively. Both SSFs show obvious peaks at the  $\tilde{M}$  points, which is a typical characteristic of the stripe order as shown in Fig. 4(i). Thus, this further confirms that the stripe-A phase extends to a large region in the phase diagram. In Fig. 4(d), we illustrate the SSF for  $\alpha = 0.3\pi$ ,  $\beta = 0$  for one of the phases that does not exist in the HK limit, which also shows distinct peaks at the  $\tilde{M}$  points, so the phase containing this point is also a stripe phase and we denote it the stripe-C phase in the phase diagram.

Although the singularities in  $-\partial^2 E_0 / \partial \alpha^2$  and  $-\partial^2 E_0 / \partial \beta^2$  show that there are phase transitions between stripe A, stripe B, and stripe C (see Appendix A for details), the differences between these phases cannot be seen from the SSFs, which show the same characteristic wave vector [Figs. 4(a)–4(d)]. In fact, the most commonly used physical quantity to distinguish different quantum phases is the order parameter. For the magnetically ordered phases, such as the stripe phases discussed here, the order parameter can be defined as  $\mathbf{m}(\mathbf{Q}) = \frac{1}{N} \sum_i \langle \mathbf{S}_i | \mathbf{S}_i | \Omega \rangle e^{i\mathbf{Q} \cdot \mathbf{r}_i}$ , where  $|\Omega\rangle$  is the GS and  $\mathbf{Q}$  is the characteristic wave vector. Thus, both the ordering wave vector and the moment direction are the defining characteristics. The difference between the stripe-A, stripe-B, and stripe-C phases lies in that they have different moment directions, which we will discuss in detail later.

When we carefully examine the SSF near  $\beta = 0.5\pi$ , we find that the SSF is obviously different from those of the stripe phases. As shown in Fig. 4(e) for  $\alpha = 0.3\pi$  and  $\beta = 0.5\pi$ , besides the peaks at the  $\tilde{M}$  points, the SSF also shows significant intensities along the boundary of the Brillouin zone (BZ). To clarify whether there is another magnetically ordered phase near  $\beta = 0.5\pi$ , we use the basin-hopping technique again to search for the possible spin order for  $\alpha = 0.3\pi$  and  $\beta = 0.5\pi$  on a  $12 \times 12$  lattice. The spin configuration is depicted in Fig. 5(a), which exhibits a modulated stripe order. For this modulated stripe order, the spins are FM along a next-NN direction and the spin orientation of the FM chains are modulated along the direction perpendicular to the FM

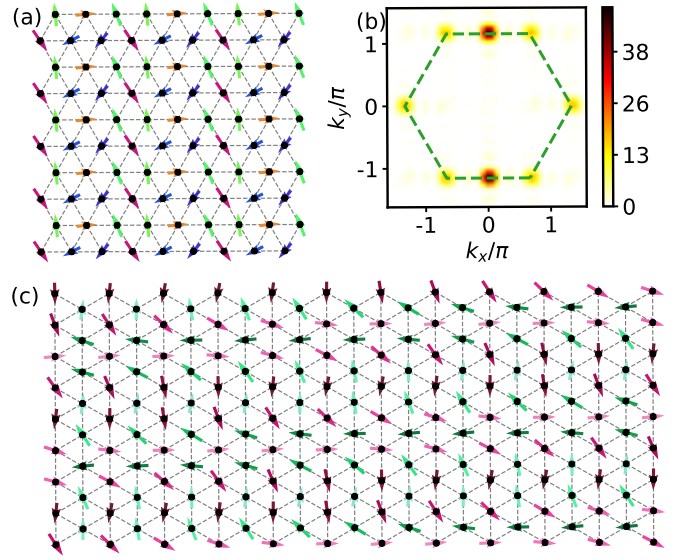


FIG. 5. (a) Spin configuration obtained from basin-hopping optimization for  $\alpha = 0.3\pi$ ,  $\beta = 0.5\pi$  in a  $12 \times 12$  cluster. (b) SSF corresponding to the spin configuration shown in (a). (c) Spin configuration obtained from the classical Monte Carlo calculations in a  $24 \times 24$  cluster.

chains to form a structure with a period of six. As illustrated in Fig. 5(b), the SSF of this classical six-chain stripe order shows clear peaks at the  $\tilde{K}$  points in addition to those at the  $\tilde{M}$  points, which is consistent with the characteristic of the SSF in Fig. 4(e) calculated by the ED. We further perform a classical Monte Carlo simulations (see Sec. II C) on a  $24 \times 24$  lattice to check the stability of the modulated stripe order in large-size systems, and the GS spin configuration is shown in Fig. 5(c). We find that the spin arrangement is still a modulated stripe order, although the spin orientations are also modulated along the FM chains in addition to a larger modulated period perpendicular to the chains. Thus, we unveil an unnoticed phase in the region between the stripe-A and stripe-C phases and term it the modulated stripe order phase.

For the other two phases with large areas and mainly located in the  $J < 0$  region of the phase diagram, we show the SSFs of two representative points with  $\alpha = 0.3\pi$ ,  $\beta = 1.3\pi$  and  $\alpha = 0.7\pi$ ,  $\beta = 1.65\pi$  in Figs. 4(f) and 4(g), respectively. The SSFs are peaked at the  $\tilde{\Gamma}$  point of the first BZ, so both phases have FM orders and they are denoted FM-B and FM-C in Fig. 2. We note that there are two special points with  $\Gamma = \pm 1$  ( $J = K = 0$ ) in the two FM phases, which are located at the phase boundary in the classical phase diagram [64]. Thus, it is worthy to discuss the properties of the pure  $\Gamma$  models in detail, and we perform an analysis based on the basin-hopping global optimization and classical Monte Carlo methods. For  $\Gamma = +1$ , apart from the FM GS with the spin orientation lying in the lattice plane, we also found disordered states having the same energy as the FM state (see Appendix D for details). For  $\Gamma = -1$ , in addition to the FM order perpendicular to the lattice plane, there are also several noncollinear magnetic orders energetically degenerate with the FM state (see Appendix D for details). However, according to our ED calculations, for the quantum model, quantum fluctuations select the FM ordered states as the GS out of the degenerate manifolds of

classical states. This selection of states among the degenerate classical GSs is the so-called order-by-disorder mechanism, which has previously been applied in a number of insulating magnets, especially in cases where frustration leads to a degenerate manifold of classical GS configurations that is broken by quantum fluctuations [71–75].

According to the above analyses, we find that, unlike the case for the honeycomb lattice, the Kitaev interactions on the triangular lattice do not give rise to QSL states. Here, the large coordination number plays a key role in stabilizing the classical magnetic orders, although the geometric and exchange frustrations coexist in the triangular lattice  $J$ - $K$ - $\Gamma$  model. However, the SSF for the quantum phase in a small region around the point with  $J = K = 0$  and  $\Gamma = 1$  illustrated in Fig. 4(h) exhibits high intensities at both  $\tilde{\Gamma}$  and  $\tilde{M}$  points, and it seems impossible for a classical magnetically ordered state to satisfy these two wave vectors simultaneously, so we infer that this quantum phase is a QSL candidate.

So far, we have determined every phase in the parameter space but there are still two problems should be addressed: First, why there are phase transitions between the phases with the same type of classical orders, such as the phase transitions between FM phases or stripe phases, and why the FM and stripe phases of the HK model are the phase boundaries in the global phase diagram of  $J$ - $K$ - $\Gamma$  model; second, what other important characteristics of the possible QSL phase in the phase diagram can be used to help us understand its properties more deeply. In the following, we will address these problems.

### B. FM phases

To have a better understanding of the phase transitions between these FM phases, we first study the classical  $J$ - $K$ - $\Gamma$  model where the spin operators are viewed as unit vectors in three-dimensional space. For classical FM states, all spins are aligned in parallel and the energy per lattice site is given by

$$E_{\text{FM}}^c = (3J + K) + 2\Gamma(v^x v^y + v^y v^z + v^z v^x), \quad (16)$$

where  $v^x$ ,  $v^y$ ,  $v^z$  are the three components of the classical moment vector. On this level, the moment direction of the FM state is determined solely by  $\Gamma$ , so the problem becomes finding the global minimum and maximum of the multi-variable function  $f(v^x, v^y, v^z) = v^x v^y + v^y v^z + v^z v^x$  with the constraint  $|v| = 1$ .  $f(v^x, v^y, v^z)$  takes the maximum value  $f_{\text{max}} = 1$  at  $v^x = v^y = v^z = \pm 1/\sqrt{3}$  and minimum value  $f_{\text{min}} = -0.5$  when the conditions  $v^x + v^y + v^z = 0$  and  $|v| = 1$  are fulfilled. The condition  $v^x + v^y + v^z = 0$  specifies a plane perpendicular to the [111] direction, and considering the reference frame shown in Fig. 1(b) it is actually the plane of the triangular lattice. That is to say, for  $\Gamma > 0$  the ordered moment of the classical FM state prefers to lie in the lattice plane, while for  $\Gamma < 0$  the ordered moment would be perpendicular to the lattice plane. This is the reason that there is a phase transition between the FM-B and FM-C phases, since the dependence of the GS energy on the interaction parameters is different for the two FM phases, and the phase boundary is the line with  $\Gamma = 0$ .

To confirm the consistency between the above classical analyses and the ED results, we use the spin coherent state to extract the moment directions of these FM phases from

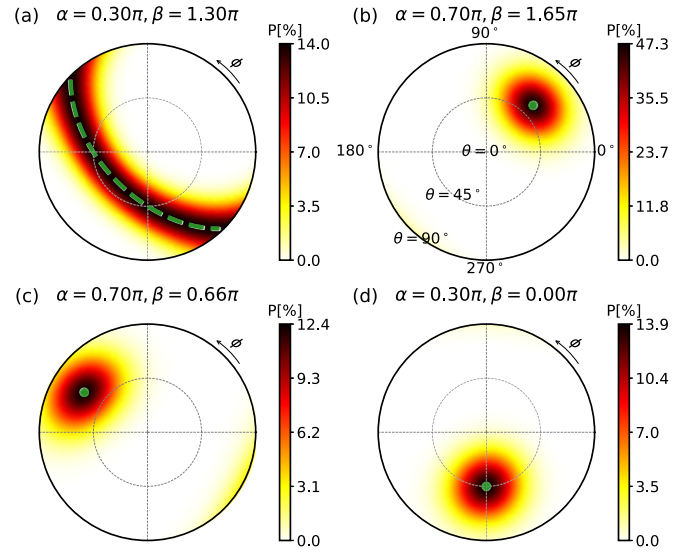


FIG. 6. Maps of the probabilities of the cluster spin coherent states given by Eq. (8) in exact cluster GSs for (a) FM-B, (b) FM-C, (c) stripe-A, and (d) stripe-C phases. The radial and polar coordinates give the angles  $\theta$  and  $\phi$ , which are spherical angles with respect to the reference frame shown in Fig. 1(b). The green dashed line and solid circles mark the ordered moment directions for the classical states. Note that the GSs are twofold degenerate for the FM-C phase and six-fold degenerate for the stripe-A and stripe-C phases, so the total probabilities for all of these phases are approximate to 1.

our ED cluster GSs [65]. Since the cluster spin coherent state defined in Eq. (8) is captured only by a single pair of  $(\theta, \phi)$  for the collinear states, it is easy to determine the directions of the FM orders by inspecting the probability map  $P(\theta, \phi) = |\langle \Psi(\theta, \phi) | \text{GS} \rangle|^2$ . As shown in Fig. 6(a), for the FM-B phase, the peaks of the probability form a ring, indicating that the moment is constrained to a plane with all directions degenerate. To compare with the classical results, we plot the classical magnetic moment directions with the green dashed line in Fig. 6(a) and find that the probability centers on the classical magnetic moment directions. For the FM-C phase, the probability map is clearly peaked at specific directions, which are also consistent with the classical results marked by the green solid circle in Fig. 6(b). Moreover, the large overlaps between the exact cluster GSs and FM cluster spin coherent states again provide solid evidence that the ED results are consistent with the classical analyses.

### C. Stripe phases

Inspired by the above discussion of the FM phases, we here perform the same analysis for the stripe phases. For the stripe order, there are three degenerated spin configurations in real space, designated as stripe  $x$ , stripe  $y$ , and stripe  $z$ , where the FM chains are along the  $x$ -bond,  $y$ -bond, and  $z$ -bond directions, respectively. For simplicity, we take the stripe- $x$  configuration as an example, and the other two configurations can be obtained by analogy. The energy per lattice site for the stripe- $x$  configuration is

$$E_{\text{stripe-x}}^c = -(J + K) + 2Kv^x v^x + 2\Gamma(v^y v^z - v^z v^x - v^x v^y). \quad (17)$$



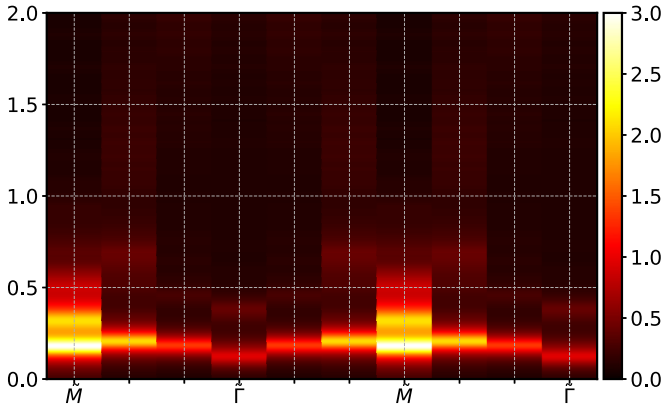


FIG. 7. DSF  $A(\mathbf{k}, \omega)$  for  $\alpha = 0.05\pi$ ,  $\beta = 0.1\pi$  in the QSL phase. The path  $\tilde{M} - \tilde{\Gamma} - \tilde{M} - \tilde{\Gamma}$  is shown in Fig. 4(i).

The ordered moment direction of the classical stripe order is determined by the interaction parameters  $K$  and  $\Gamma$ . In general ( $K, \Gamma \neq 0$ ),  $E_{\text{stripe}-x}^c$  has six extreme points where the first derivatives with respect to  $v_x$ ,  $v_y$ , and  $v_z$  are equal to zero. Here we give three of them explicitly and the other three are opposite to the given ones,

$$v_0 : v_0^y = -v_0^z = 1/\sqrt{2}, \quad v_0^x = 0, \quad (18a)$$

$$v_1 : v_1^y = v_1^z = f_1(K, \Gamma), \quad v_1^x = g_1(K, \Gamma)v_1^y, \quad (18b)$$

$$v_2 : v_2^y = v_2^z = f_2(K, \Gamma), \quad v_2^x = g_2(K, \Gamma)v_2^y, \quad (18c)$$

where

$$f_{1,2}(K, \Gamma) = \frac{|\Gamma|}{\sqrt{4\lambda_{1,2}(\lambda_{1,2} + \Gamma) + 3\Gamma^2}},$$

$$g_{1,2}(K, \Gamma) = (2\lambda_{1,2} + \Gamma)/\Gamma,$$

with

$$\lambda_1 = -(\Gamma + 2K - \sqrt{9\Gamma^2 - 4\Gamma K + 4K^2})/4,$$

$$\lambda_2 = -(\Gamma + 2K + \sqrt{9\Gamma^2 + 4\Gamma K + 4K^2})/4.$$

In the HK limit, for  $K > 0$ , it can be clearly seen from Eq. (17) that  $E_{\text{stripe}-x}^c$  takes minimum value at  $v^x = 0$  which means that the moments of the stripe- $x$  configuration prefer to lie in the  $yz$  plane. An infinitesimal positive  $\Gamma$  would fix the ordered moment to the  $v_0$  direction, whereas the negative  $\Gamma$  drives it to the  $v_1$  direction. Thus, there is a phase transition between the stripe-A and stripe-C phases, as the GS energies have different dependence on the interaction parameters for the two stripe phases, and the phase boundary is the line with  $\Gamma = 0$ .

To confirm that the classical analysis is consistent with our ED calculations, we use the spin coherent states again to extract the ordered moment directions of the ED GSs in these stripe phases. For brevity, we here only construct cluster spin coherent state based on the stripe- $x$  configuration and present the resulting probability maps in Figs. 6(c) and 6(d) for the stripe-A and stripe-C phases, respectively. We can see that there are large overlaps between the exact cluster GS and stripe cluster spin coherent state, which indicates that the results based on the ED calculation are consistent with the classical analysis.

#### D. Possible QSL

Although the GSs of the pure Heisenberg, Kitaev, and  $\Gamma$  models are not QSL, the interplay of the Heisenberg, Kitaev, and  $\Gamma$  interactions may induce a possible QSL phase near the  $\Gamma = 1$  limit as discussed above according to the SSF. To have further understanding of the nature of this quantum phase that does not exist in the classical phase diagram [64], we also calculate the DSF  $A(\mathbf{k}, \omega)$ , which in general can provide some critical information about the properties of a QSL. A typical  $A(\mathbf{k}, \omega)$  profile is shown in Fig. 7. A significant feature one can see is that the whole spectrum is a broad continuum, which is a characteristic of QSL originating from the fractionalization of the  $S = 1$  spin excitations. Thus, the DSF gives further evidence that this quantum phase is a QSL. The DSF also shows another feature that the periodicity of its lower edge is doubled (i.e.,  $\tilde{M}-\tilde{\Gamma}$  forms a period instead of the usual  $\tilde{M}-\tilde{M}$ ), which is a signature of the translational symmetry fractionalization of a  $Z_2$  spin liquid [76–78]. Moreover, we find that there is an obvious gap in the DSF. Thus, combined with all of the above results, we propose that the GS of quantum  $J$ - $K$ - $\Gamma$  model at the green area of the phase diagram in Fig. 2 is a gapped  $Z_2$  QSL.

#### IV. SUMMARY

In summary, we carry out a comprehensive study of the  $J$ - $K$ - $\Gamma$  model on a triangular lattice in the full parameter space and map out its global phase diagram by use of a combination of the ED, the classical Monte Carlo simulation, and analytical analyses. We find that there are five quantum phases in the limit of  $\Gamma = 0$ . Among them, the  $120^\circ$  Néel, the dual Néel, and one of the stripe phases extend into the region with  $\Gamma \neq 0$ . However, the other stripe and the FM phases are unstable in response to an infinitesimal  $\Gamma$  interaction. Due to the introduction of the  $\Gamma$  term, five additional phases emerge, including two FM phases, one stripe, one modulated stripe, and a possible QSL. We also elaborate that the pure  $\Gamma$  model has a FM GS and the AFM Kitaev model a stripe GS, which are selected by the order-by-disorder mechanism from the degenerate classical GSs. Our study of the global phase diagram on a generic spin model paves the way for future studies of a large group of triangular transition-metal materials with an appreciable spin-orbit coupling and electronic correlations.

#### ACKNOWLEDGMENTS

This work was supported by the National Natural Science Foundation of China (Grants No. 11674158, No. 11774152, No. 11774300, No. 12004191, and No. 12074175, National Key Projects for Research and Development of China (Grant No. 2016YFA0300401) and Natural Science Foundation of Jiangsu Province, China (Grant No. BK20200738).

#### APPENDIX A: PHASE BOUNDARIES IN THE ZERO-TEMPERATURE QUANTUM PHASE DIAGRAM

As mentioned in the main text, the phase boundaries are determined by the locations of singularities in  $-\partial^2 E_0/\partial\alpha^2$  and  $-\partial^2 E_0/\partial\beta^2$ , based on the ED calculations. Some representative curves are shown in Fig. 8. In Fig. 8(a) for  $\alpha = 0.05\pi$ ,



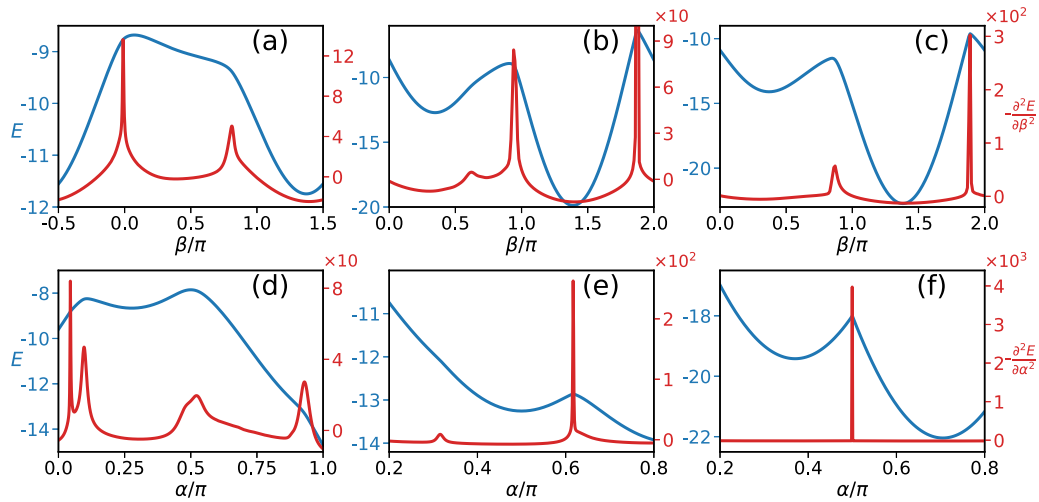


FIG. 8. GS energies and their second derivatives versus  $\alpha$  or  $\beta$  for six representative paths in the phase diagram. The ED calculations are performed on a  $4 \times 6$  cluster with periodic boundary condition. The blue lines are the GS energies and the red lines are the second derivatives. In (a)–(c),  $\alpha$  is fixed to  $0.05\pi$ ,  $0.3\pi$ , and  $0.75\pi$ , respectively. In (d)–(f),  $\beta$  is fixed to 0,  $0.5\pi$ , and  $1.5\pi$ , respectively.

the second derivative of  $E_0$  versus  $\beta$  has two peaks located at  $\beta = -0.01\pi$  and  $\beta = 0.81\pi$ , which are the phase boundaries between the FM-B and QSL phases. As we increase  $\alpha$  to  $0.3\pi$ , there are three singularities in the second derivatives [see Fig. 8(b)]. The small peak at  $\beta = 0.62\pi$  indicates the phase transition from modulated stripe to stripe A, while the other two sharp peaks at  $\beta = 0.94\pi$  and  $\beta = 1.87\pi$  originate from the phase transitions from stripe A to FM-B and from FM-B to stripe C, respectively. Figure 8(c) shows the case for

$\alpha = 0.75\pi$ , where the two peaks located at  $\beta = 0.87\pi$  and  $\beta = 1.89\pi$  signify the phase transitions between stripe A and FM-C. On the other hand, we can also fix  $\beta$  to detect the phase transitions with varying  $\alpha$  and the corresponding results are shown in Figs. 8(d)–8(f). In Fig. 8(d),  $\beta$  equals 0, the first two sharp peaks at  $\alpha = 0.045\pi$  and  $\alpha = 0.097\pi$  reveal the phase transitions from FM-B to QSL and further to stripe C. The peak at about  $\alpha = 0.5\pi$  is due to the phase transition from stripe C to stripe A. The last singularity at  $\alpha = 0.93\pi$  marks

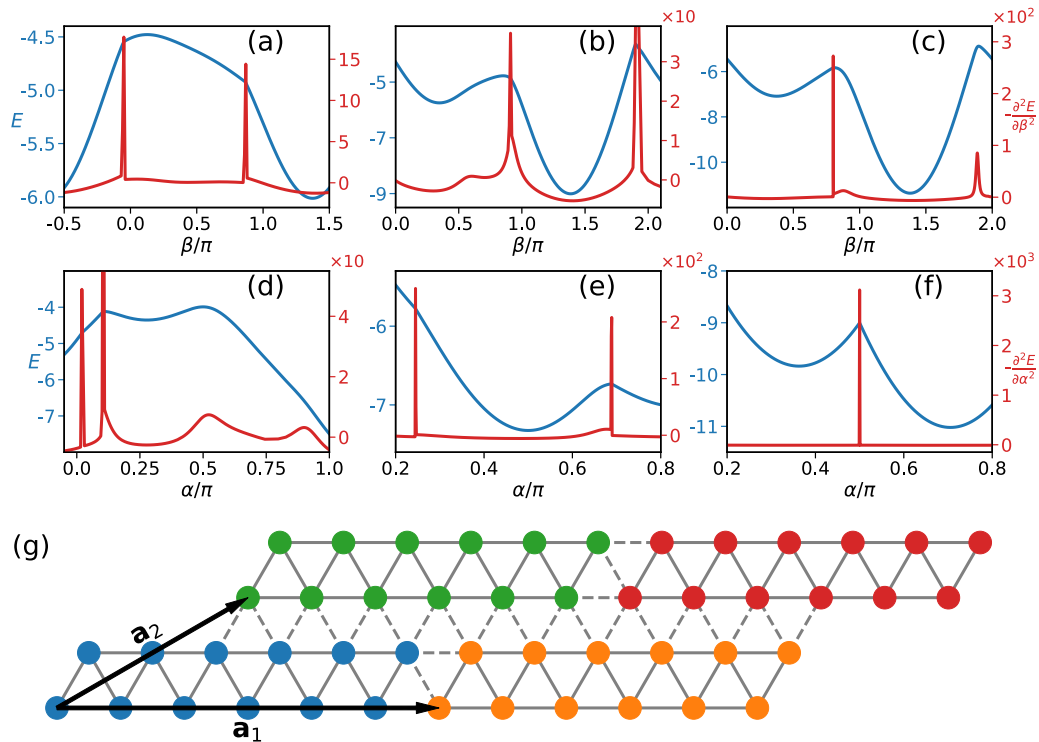


FIG. 9. GS energies and their second derivatives versus  $\alpha$  or  $\beta$  along the same paths shown in Fig. 8. The blue lines are the GS energies and the red lines are the second derivatives. In (a)–(c),  $\alpha$  is fixed to  $0.05\pi$ ,  $0.2\pi$ , and  $0.75\pi$ , respectively. In (d)–(f),  $\beta$  is fixed to 0,  $0.5\pi$ , and  $1.5\pi$ , respectively. (g) The  $2 \times 6$  cluster as well as the periodic boundary condition that is used to perform the ED calculations.

the phase boundary between stripe A and FM-C. In Fig. 8(e), we show the phase transition between modulated stripe and  $120^\circ$  Néel as well as the phase transition from  $120^\circ$  Néel to stripe A. Here,  $\beta$  is fixed to  $0.5\pi$  and the transitions occur at  $\alpha = 0.32\pi$  and  $\alpha = 0.62\pi$ , respectively. Last but not least, we show there are phase transitions between these different FM phases. In Fig. 8(f) where  $\beta = 1.5\pi$ , the sharp peak at  $\alpha = 0.5\pi$  shows that the FM-A phase for the HK model is a phase-transition boundary, infinitesimal  $\Gamma$  interaction will cause phase transitions to other FM phases which have different moment directions from the FM-A phase.

## APPENDIX B: EFFECTS OF SYSTEM SIZE ON THE PHASE BOUNDARIES

To study the effects of system size on the zero-temperature quantum phase diagram, we also carry out ED calculations on a  $2 \times 6$  cluster with periodic boundary condition, see Fig. 9(g) for the shape of the cluster as well as the form of the boundary condition. This cluster and the boundary condition are compatible with most of the magnetic orders, such as FM, stripe,  $120^\circ$  Néel, dual Néel, and six-chain modulated stripe shown in Fig. 5(a).

In Figs. 9(a)–9(c), the  $\alpha$  parameter is fixed to be  $0.05\pi$ ,  $0.2\pi$ , and  $0.75\pi$ , respectively. In Figs. 9(d)–9(f), the  $\beta$  parameter is fixed to be 0,  $0.5\pi$ , and  $1.5\pi$ , respectively. The singularities in Figs. 9(a)–9(f) are consistent with the results of the  $4 \times 6$  cluster shown in Figs. 8(a)–8(f) even though the positions of the phase boundaries are slightly shifted. It is worth noting that, in Fig. 9(b) the  $\beta$  parameter is fixed to  $0.2\pi$  while in Fig. 8(b)  $\beta = 0.3\pi$ , since the region of the  $120^\circ$  Néel phase extends to a larger area for the  $2 \times 6$  cluster, which leads to that  $\beta = 0.3\pi$  is still in the  $120^\circ$  Néel phase. Thus, in comparison with the results for the  $4 \times 6$  cluster, we find that different system sizes do not change the phase

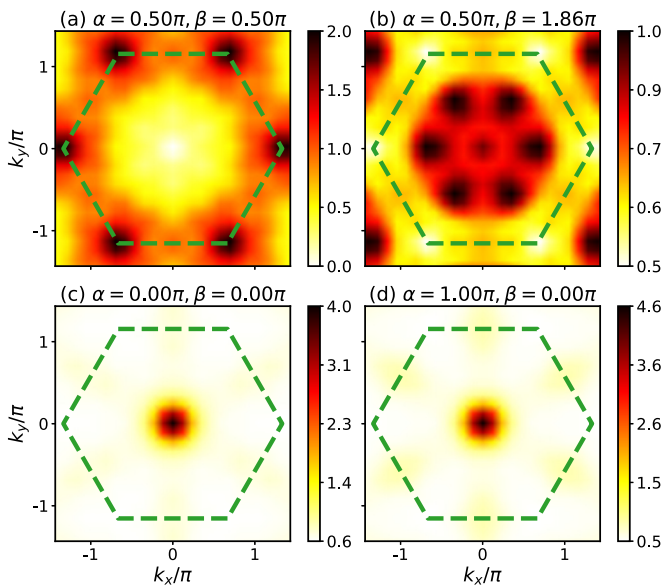


FIG. 10. (a) and (b) are the representative SSF profiles for  $120^\circ$  Néel and dual Néel phases, respectively. (c) and (d) are the SSF profiles for the pure  $\Gamma$  models with  $\Gamma = \pm 1$ , respectively.

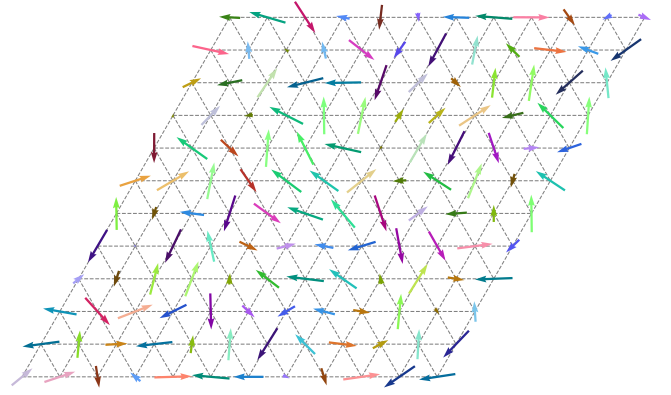


FIG. 11. Typical disordered GS for  $J = K = 0$ ,  $\Gamma = 1$ . For clarity, the equal spin vectors are marked with the same color and the arrows denote the projections of the three-dimensional vectors to the  $xy$  plane.

diagram qualitatively and only affect the locations of the phase boundaries.

## APPENDIX C: SUPPLEMENTS OF THE SSF FROM THE ED CALCULATIONS

Here we provide additional SSF profiles as a supplement to these profiles shown in the main text. For the classical  $120^\circ$  Néel state, the SSF has high intensity at the corner of the first BZ, i.e.,  $\tilde{K}$  points and the SSF peaked at the middle points of  $\tilde{\Gamma}$  and  $\tilde{K}$ 's for the dual Néel state. Figures 10(a) and 10(b) show the SSF profiles calculated from our ED GS at  $\alpha = 0.5\pi$ ,  $\beta = 0.5\pi$  and  $\alpha = 0.5\pi$ ,  $\beta = 1.85\pi$ , which are located at the  $120^\circ$  Néel phase and dual Néel phase, respectively. For both profile, the points with highest intensity are consistent with the classical analyses.

In the main text, we argue that the GSs of the pure  $\Gamma$  models are FM ordered states. Here we provide the SSFs for  $\Gamma = \pm 1$  in Figs. 10(c) and 10(d). Both SSFs have high

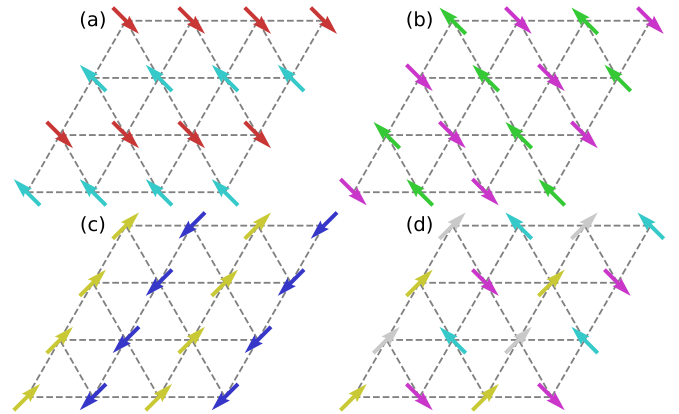


FIG. 12. Typical classical GS spin configurations for  $J = K = 0$ ,  $\Gamma = -1$ . The spin vectors are projected to the  $xy$  plane and different vectors are represented by different colors. (a)–(c) Stripe ordered states. The directions for the cyan, red, pink, green, yellow, and blue arrows are  $[\bar{1}11]$ ,  $[1\bar{1}\bar{1}]$ ,  $[1\bar{1}\bar{1}]$ ,  $[\bar{1}11]$ ,  $[1\bar{1}\bar{1}]$ , and  $[\bar{1}11]$ , respectively. (d) Noncollinear state. The directions for the yellow, gray, pink, cyan arrows are  $[1\bar{1}\bar{1}]$ ,  $[111]$ ,  $[1\bar{1}\bar{1}]$ , and  $[\bar{1}11]$ , respectively.

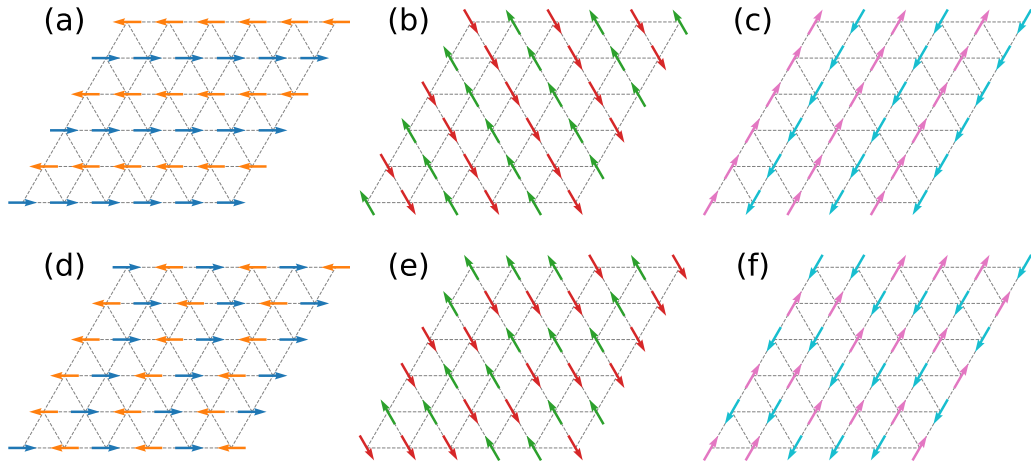


FIG. 13. Classical stripe and nematic GS spin configurations for  $J = \Gamma = 0$ ,  $K = 1$ . (a)–(c) Stripe states. (d)–(f) Nematic states.

intensities at the  $\tilde{\Gamma}$  points, which is a typical characteristic of FM states.

#### APPENDIX D: CLASSICAL GS CONFIGURATIONS FOR SOME SPECIAL INTERACTION PARAMETERS

##### 1. $J = K = 0$ , $\Gamma = 1$

For the pure positive  $\Gamma$  model, the classical GSs are highly degenerate, including the FM state as well as states with no long-range order. The ordered moments of the FM state lie in the lattice plane. Fig. 11 shows a typical spin configuration of those disordered states that have the same energy as the FM state.

##### 2. $J = K = 0$ , $\Gamma = -1$

For the pure negative  $\Gamma$  model, we found several energetically degenerate states as the classical GSs, including the FM state, stripe states, and a noncollinear state. The ordered moment of the FM state is perpendicular to the lattice plane. As for the stripe states, there are three degenerate spin configurations as shown in Figs. 12(a)–12(c) and the moment directions for the cyan, red, pink, green, yellow, and blue

arrows are  $[\bar{1}11]$ ,  $[1\bar{1}\bar{1}]$ ,  $[1\bar{1}1]$ ,  $[\bar{1}1\bar{1}]$ ,  $[11\bar{1}]$ , and  $[\bar{1}\bar{1}1]$ , respectively. Apart from these collinear states, a noncollinear state also exists as the classical GS. The magnetic unit-cell contains four lattice sites, and the moment directions for the yellow, gray, pink, cyan arrows in Fig. 12(d) are  $[1\bar{1}\bar{1}]$ ,  $[111]$ ,  $[\bar{1}\bar{1}1]$ , and  $[\bar{1}11]$ , respectively.

##### 3. $J = \Gamma = 0$ , $K = 1$

The GSs for the classical AFM Kitaev model are also degenerate involving three types of nematically ordered states and three stripe-ordered states. For the stripe-ordered states shown in Figs. 13(a)–13(c), the corresponding ordered moments lie in the  $yz$ ,  $xz$ , and  $xy$  planes, respectively. For the nematically ordered state shown in Fig. 13(d), the spins form AFM chains along the  $x$ -bond direction and the moment direction for the blue arrows are  $[100]$ . Different AFM chains are decoupled in the nematic state. Similarly, the AFM chains are along the  $y$ -bond and  $z$ -bond directions for Fig. 13(e) and Fig. 13(f), respectively. The direction for the green arrows in Fig. 13(e) and pink arrows in Fig. 13(f) are  $[010]$  and  $[001]$ , respectively.

- 
- [1] P. Anderson, *Mater. Res. Bull.* **8**, 153 (1973).
  - [2] S. R. White and A. L. Chernyshev, *Phys. Rev. Lett.* **99**, 127004 (2007).
  - [3] L. Capriotti, A. E. Trumper, and S. Sorella, *Phys. Rev. Lett.* **82**, 3899 (1999).
  - [4] B. Bernu, P. Lecheminant, C. Lhuillier, and L. Pierre, *Phys. Rev. B* **50**, 10048 (1994).
  - [5] D. A. Huse and V. Elser, *Phys. Rev. Lett.* **60**, 2531 (1988).
  - [6] P. H. Y. Li, R. F. Bishop, and C. E. Campbell, *Phys. Rev. B* **91**, 014426 (2015).
  - [7] Z. Zhu and S. R. White, *Phys. Rev. B* **92**, 041105(R) (2015).
  - [8] W.-J. Hu, S.-S. Gong, W. Zhu, and D. N. Sheng, *Phys. Rev. B* **92**, 140403(R) (2015).
  - [9] D.-V. Bauer and J. O. Fjærestad, *Phys. Rev. B* **96**, 165141 (2017).
  - [10] Y. Iqbal, W.-J. Hu, R. Thomale, D. Poilblanc, and F. Becca, *Phys. Rev. B* **93**, 144411 (2016).
  - [11] R. Kaneko, S. Morita, and M. Imada, *J. Phys. Soc. Jpn* **83**, 093707 (2014).
  - [12] S. N. Saadatmand and I. P. McCulloch, *Phys. Rev. B* **94**, 121111(R) (2016).
  - [13] S.-S. Gong, W. Zhu, J.-X. Zhu, D. N. Sheng, and K. Yang, *Phys. Rev. B* **96**, 075116 (2017).
  - [14] Z. Zhu, P. A. Maksimov, S. R. White, and A. L. Chernyshev, *Phys. Rev. Lett.* **120**, 207203 (2018).
  - [15] Q. Luo, S. Hu, B. Xi, J. Zhao, and X. Wang, *Phys. Rev. B* **95**, 165110 (2017).
  - [16] S. Hu, W. Zhu, S. Eggert, and Y.-C. He, *Phys. Rev. Lett.* **123**, 207203 (2019).
  - [17] F. Ferrari and F. Becca, *Phys. Rev. X* **9**, 031026 (2019).

- [18] M. Wu, D.-X. Yao, and H.-Q. Wu, [arXiv:2008.08751](#).
- [19] A. Kitaev, *Ann. Phys.* **321**, 2 (2006).
- [20] G. Khaliullin, *Prog. Theor. Phys. Suppl.* **160**, 155 (2005).
- [21] G. Jackeli and G. Khaliullin, *Phys. Rev. Lett.* **102**, 017205 (2009).
- [22] J. Chaloupka, G. Jackeli, and G. Khaliullin, *Phys. Rev. Lett.* **105**, 027204 (2010).
- [23] M. Hermanns, I. Kimchi, and J. Knolle, *Annu. Rev. Condens. Matter Phys.* **9**, 17 (2018).
- [24] J. Chaloupka, G. Jackeli, and G. Khaliullin, *Phys. Rev. Lett.* **110**, 097204 (2013).
- [25] H.-C. Jiang, Z.-C. Gu, X.-L. Qi, and S. Trebst, *Phys. Rev. B* **83**, 245104 (2011).
- [26] J. Reuther, R. Thomale, and S. Trebst, *Phys. Rev. B* **84**, 100406(R) (2011).
- [27] J. Osorio Iregui, P. Corboz, and M. Troyer, *Phys. Rev. B* **90**, 195102 (2014).
- [28] M. Gohlke, R. Verresen, R. Moessner, and F. Pollmann, *Phys. Rev. Lett.* **119**, 157203 (2017).
- [29] J. G. Rau, Eric Kin-Ho Lee, and H.-Y. Kee, *Phys. Rev. Lett.* **112**, 077204 (2014).
- [30] S. M. Winter, Y. Li, H. O. Jeschke, and R. Valentí, *Phys. Rev. B* **93**, 214431 (2016).
- [31] W. Wang, Z.-Y. Dong, S.-L. Yu, and J.-X. Li, *Phys. Rev. B* **96**, 115103 (2017).
- [32] S. M. Winter, A. A. Tsirlin, M. Daghofer, J. van den Brink, Y. Singh, P. Gegenwart, and R. Valentí, *J. Phys. Condens. Matter* **29**, 493002 (2017).
- [33] H. Takagi, T. Takayama, G. Jackeli, G. Khaliullin, and S. E. Nagler, *Nat. Rev. Phys.* **1**, 264 (2019).
- [34] I. Kimchi and A. Vishwanath, *Phys. Rev. B* **89**, 014414 (2014).
- [35] I. Rousochatzakis, U. K. Rössler, J. van den Brink, and M. Daghofer, *Phys. Rev. B* **93**, 104417 (2016).
- [36] T. Dey, A. V. Mahajan, P. Khuntia, M. Baenitz, B. Koteswararao, and F. C. Chou, *Phys. Rev. B* **86**, 140405(R) (2012).
- [37] R. Kumar, D. Sheptyakov, P. Khuntia, K. Rolfs, P. G. Freeman, H. M. Rønnow, T. Dey, M. Baenitz, and A. V. Mahajan, *Phys. Rev. B* **94**, 174410 (2016).
- [38] Y. Li, H. Liao, Z. Zhang, S. Li, F. Jin, L. Ling, L. Zhang, Y. Zou, L. Pi, Z. Yang, J. Wang, Z. Wu, and Q. Zhang, *Sci. Rep.* **5**, 16419 (2015).
- [39] Y. Li, G. Chen, W. Tong, L. Pi, J. Liu, Z. Yang, X. Wang, and Q. Zhang, *Phys. Rev. Lett.* **115**, 167203 (2015).
- [40] Z. Ma, J. Wang, Z.-Y. Dong, J. Zhang, S. Li, S.-H. Zheng, Y. Yu, W. Wang, L. Che, K. Ran, S. Bao, Z. Cai, P. Čermák, A. Schneidewind, S. Yano, J. S. Gardner, X. Lu, S.-L. Yu, J.-M. Liu, S. Li, J.-X. Li *et al.*, *Phys. Rev. Lett.* **120**, 087201 (2018).
- [41] F. A. Cevallos, K. Stolze, T. Kong, and R. Cava, *Mater. Res. Bull.* **105**, 154 (2018).
- [42] J. Wen, S.-L. Yu, S. Li, W. Yu, and J.-X. Li, *npj Quantum Mater.* **4**, 12 (2019).
- [43] Y.-D. Li, X. Wang, and G. Chen, *Phys. Rev. B* **94**, 035107 (2016).
- [44] Y. Shen, Y.-D. Li, H. Wo, Y. Li, S. Shen, B. Pan, Q. Wang, H. C. Walker, P. Steffens, M. Boehm, Y. Hao, D. L. Quintero-Castro, L. W. Harriger, M. D. Frontzek, L. Hao, S. Meng, Q. Zhang, G. Chen, and J. Zhao, *Nature* **540**, 559 (2016).
- [45] J. A. M. Paddison, M. Daum, Z. Dun, G. Ehlers, Y. Liu, M. B. Stone, H. Zhou, and M. Mouriagal, *Nat. Phys.* **13**, 117 (2016).
- [46] Y. Xu, J. Zhang, Y. S. Li, Y. J. Yu, X. C. Hong, Q. M. Zhang, and S. Y. Li, *Phys. Rev. Lett.* **117**, 267202 (2016).
- [47] I. Kimchi, A. Nahum, and T. Senthil, *Phys. Rev. X* **8**, 031028 (2018).
- [48] J. Iaconis, C. Liu, G. B. Halász, and L. Balents, *SciPost Phys.* **4**, 003 (2018).
- [49] E. Parker and L. Balents, *Phys. Rev. B* **97**, 184413 (2018).
- [50] J. Xing, L. D. Sanjeeva, J. Kim, G. R. Stewart, M.-H. Du, F. A. Reboredo, R. Custelcean, and A. S. Sefat, *ACS Mater. Lett.* **2**, 71 (2019).
- [51] J. Xing, L. D. Sanjeeva, J. Kim, W. R. Meier, A. F. May, Q. Zheng, R. Custelcean, G. R. Stewart, and A. S. Sefat, *Phys. Rev. Materials* **3**, 114413 (2019).
- [52] R. Sarkar, P. Schlender, V. Grinenko, E. Haeussler, P. J. Baker, T. Doert, and H.-H. Klauss, *Phys. Rev. B* **100**, 241116(R) (2019).
- [53] W. Liu, Z. Zhang, J. Ji, Y. Liu, J. Li, X. Wang, H. Lei, G. Chen, and Q. Zhang, *Chin. Phys. Lett.* **35**, 117501 (2018).
- [54] K. M. Ranjith, D. Dmytriieva, S. Khim, J. Sichelschmidt, S. Luther, D. Ehlers, H. Yasuoka, J. Wosnitza, A. A. Tsirlin, H. Kühne, and M. Baenitz, *Phys. Rev. B* **99**, 180401(R) (2019).
- [55] K. M. Ranjith, S. Luther, T. Reimann, B. Schmidt, P. Schlender, J. Sichelschmidt, H. Yasuoka, A. M. Strydom, Y. Skourski, J. Wosnitza, H. Kühne, T. Doert, and M. Baenitz, *Phys. Rev. B* **100**, 224417 (2019).
- [56] L. Ding, P. Manuel, S. Bachus, F. Grubler, P. Gegenwart, J. Singleton, R. D. Johnson, H. C. Walker, D. T. Adroja, A. D. Hillier, and A. A. Tsirlin, *Phys. Rev. B* **100**, 144432 (2019).
- [57] K. Li, S.-L. Yu, and J.-X. Li, *New J. Phys.* **17**, 043032 (2015).
- [58] M. Becker, M. Hermanns, B. Bauer, M. Garst, and S. Trebst, *Phys. Rev. B* **91**, 155135 (2015).
- [59] K. Shinjo, S. Sota, S. Yunoki, K. Totsuka, and T. Tohyama, *J. Phys. Soc. Jpn.* **85**, 114710 (2016).
- [60] P. A. Maksimov, Z. Zhu, S. R. White, and A. L. Chernyshev, *Phys. Rev. X* **9**, 021017 (2019).
- [61] M. Li, N. B. Perkins, and I. Rousochatzakis, *Phys. Rev. Research* **1**, 013002 (2019).
- [62] K. Morita and T. Tohyama, *Phys. Rev. Research* **2**, 013205 (2020).
- [63] P. Kos and M. Punk, *Phys. Rev. B* **95**, 024421 (2017).
- [64] A. Catuneanu, J. G. Rau, H.-S. Kim, and H.-Y. Kee, *Phys. Rev. B* **92**, 165108 (2015).
- [65] J. Chaloupka and G. Khaliullin, *Phys. Rev. B* **94**, 064435 (2016).
- [66] K. Hukushima and K. Nemoto, *J. Phys. Soc. Jpn.* **65**, 1604 (1996).
- [67] Y. Miyatake, M. Yamamoto, J. J. Kim, M. Toyonaga, and O. Nagai, *J. Phys. C: Solid State Phys.* **19**, 2539 (1986).
- [68] B. A. Berg, *Markov Chain Monte Carlo Simulations and Their Statistical Analysis* (World Scientific, Singapore, 2004).
- [69] D. J. Wales and J. P. K. Doye, *J. Phys. Chem. A* **101**, 5111 (1997).
- [70] G. Jackeli and A. Avella, *Phys. Rev. B* **92**, 184416 (2015).
- [71] T. Oguchi, H. Nishimori, and Y. Taguchi, *J. Phys. Soc. Jpn.* **54**, 4494 (1985).
- [72] C. L. Henley, *Phys. Rev. Lett.* **62**, 2056 (1989).
- [73] O. Tchernyshyov, R. Moessner, and S. L. Sondhi, *Phys. Rev. Lett.* **88**, 067203 (2002).



- [74] A. Mulder, R. Ganesh, L. Capriotti, and A. Paramekanti, [Phys. Rev. B \*\*81\*\*, 214419 \(2010\)](#).
- [75] M. E. Zhitomirsky, M. V. Gvozdkova, P. C. W. Holdsworth, and R. Moessner, [Phys. Rev. Lett. \*\*109\*\*, 077204 \(2012\)](#).
- [76] A. M. Essin and M. Hermele, [Phys. Rev. B \*\*90\*\*, 121102\(R\) \(2014\)](#).
- [77] J.-W. Mei and X.-G. Wen, [arXiv:1507.03007](#).
- [78] Y.-D. Li, X. Yang, Y. Zhou, and G. Chen, [Phys. Rev. B \*\*99\*\*, 205119 \(2019\)](#).